LETTER

Laboratory equation of state measurements of the carbon envelopes of white dwarf stars

Andrea L. Kritcher[1], Damian C. Swift[1], Tilo Döppner[1], Benjamin Bachmann[1], Lorin X. Benedict[1], Gilbert W. Collins[1,2], Jonathan L. DuBois[1], Fred Elsner[3], Gilles Fontaine[4], Jim A. Gaffney[1], Sebastien Hamel[1], Amy Jenei[1], Walter R. Johnson[5], Natalie Kostinski[1], Dominik Kraus[6,7], Mike MacDonald[1], Brian Maddox[1], Madison E. Martin[1], Paul Neumayer[8], Abbas Nikroo[1], Joseph Nilsen[1], Bruce A. Remington[1], Didier Saumon[9], Phillip A. Sterne[1], Wendi Sweet[3], Alfredo A. Correa Tedesco[1], Heather D. Whitley[1], Roger W. Falcone[10], Siegfried H. Glenzer[11]

[1] Lawrence Livermore National Laboratory, P.O. Box 808, Livermore, California 94551-0808, USA
[2] Departments of Mechanical Engineering, Physics and Astronomy, and Laboratory for Laser Energetics, University of Rochester, Rochester, New York 14623, USA
[3] General Atomics, P.O. Box 85608, San Diego, California 92186-5608
[4] Université de Montréal, CP 6128, Succursal Centre-Ville, Montreal, QC H3C 3J7, Canada
[5] University of Notre Dame, Notre Dame, IN 46556, USA
[6] Helmholtz-Zentrum Dresden-Rossendorf, Bautzner Landstr. 400, 01328 Dresden, Germany
[7] Institute of Solid State and Materials Physics, Technische Universität Dresden, 01069 Dresden, Germany
[8] GSI Helmholtzzentrum für Schwerionenforschung GmbH, Planckstraße 1, 64291 Darmstadt, Germany
[9] Los Alamos National Laboratory, Mail Stop F663, Los Alamos, NM 87545
[10] University of California Berkeley, 2000 Carleton Street, Berkeley, CA, 94720-2284, USA
[11] SLAC National Accelerator, 2575 Sand Hill Rd, Menlo Park, CA 94025, USA

White dwarfs (WD) represent the final state of evolution for the vast majority of stars [1–3]. Certain classes of white dwarfs pulsate[4,5], leading to observable brightness variations whose analysis with theoretical stellar models uniquely probes their internal structure. Modeling of these pulsating WD stars provides stringent tests of white dwarf models and a detailed picture of the outcome of the late stages of stellar evolution [6]. However, these high energy density states are extremely difficult to access and diagnose in the laboratory and as a result theory is largely untested at these conditions. Here, we present equation of state (EOS) measurements of matter at pressures ranging from 100-450 million atmospheres, where the understanding of WD stars is sensitive to the EOS and where models show significant differences. We measure the pressure-density relationship along the principal shock Hugoniot of hydrocarbon to within five percent. The observed maximum compressibility is consistent with theoretical models that include detailed electronic structure, are used in calculations of WD stars and inertial confinement fusion (ICF) experiments[7,8], and predict an increase in compressibility due to ionization of the inner core orbitals of carbon. We also find that detailed treatment of the electronic structure and the electron degeneracy pressure are required to capture the measured shape of the pressure-density evolution for hydrocarbon before peak compression.

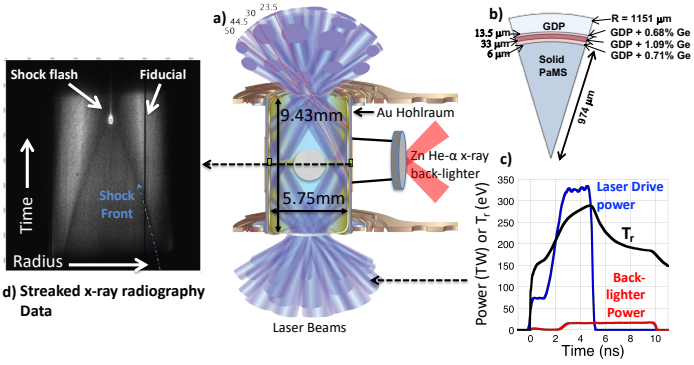

Figure 1 | Experimental configuration a) Schematic of the target showing laser beams incident on the inside of a gold hohlraum, solid spherical sample inside the hohlraum, and the x-ray backlighting configuration. b) Diagram of the sample configuration with layer thicknesses and level of Ge dopant on the right side in atom % c) Laser drive (blue) and backlighter (red) power profiles vs time. The calculated radiation temperature vs time in electron volts, T_r. (eV), is also shown (black curve). d) Streaked x-ray radiography data showing the shock front and shock flash at the core.

At pressures of a million to a billion times earth's atmosphere, (Mbar to Gbar), core electrons can affect the material compressibility by altering both the amount of stored internal energy, and the plasma pressure through ionization. At these pressures, the core electron excitation energies and the ionization are difficult to predict [9]. Depending on how these details are modeled, the equation of state along the shock Hugoniot, e.g. pressure vs compression in this work, can vary by nearly 10%[10] which is significant for white dwarf models [11]. Here we test EOS models for a hydrocarbon which is directly relevant to the modeling of white dwarf stars of the hot DQ class that contain a degenerate carbon and oxygen core surrounded by an envelope of mostly carbon [12,13]. Uncertainty in EOS and opacity models can affect the extent and properties of mixing within the convection zone which impacts the inferred surface abundances and pulsation properties of pulsating WD stars with carbon-rich envelopes [1,12–14] (see the Methods). In addition, instability growth in laboratory inertial confinement fusion experiments[7] has been shown to be sensitive to EOS modeling [15,16] with more compressible models leading to higher instability growth rates. Until now, no laboratory measurements of the shock Hugoniot have been reported at pressures exceeding ∼60 Mbar for any material, and theoretical models in this regime have not been constrained by experimental data. A

single dataset at Gbar pressures recorded in underground nuclear explosions for Aluminum[17] has uncertainty that is too large to distinguish between theoretical models.

We present laboratory equation-of-state measurements in a regime where none currently exist, enabling tests of theoretical models at pressures exceeding 100 million atmospheres. We access the atomic pressure regime >300 Mbar (see the Methods) where extreme temperatures and densities ionize inner core electron orbitals and can change the shape of the pressure vs density function ($P-\rho$) along the Hugoniot states. We resolve the shape of the Hugoniot response by measuring a continuous sequence of data points in a single shot, using a spherically convergent geometry [18–21]. The combination of small scatter and precision of the data effectively constrains EOS models. Alternate techniques such as planar dynamic compression experiments[22,23] are restricted to pressures of <60 Mbar and can only access one Hugoniot point in a single shot. Accessing the shock regime in this work required increasing the laser driver energy and using multiple coalescing shock waves to generate a single stronger shock. Operating in an intense x-ray drive environment required mitigation of sources of preheat and background from electrons and x-rays generated from the radiation drive, as well as symmetric shock generation. To interpret the experimental measurements in this high-pressure regime where the opacity at the shock front deviates significantly from the cold opacity, we developed a simultaneous density and opacity analysis method [24] (see the Methods).

These experiments were performed at the National Ignition Facility (NIF) [25] where 1 MJ of 351 nanometer laser light was delivered to the inside of a gold cylinder (hohlraum) creating an x-ray radiation bath with a maximum radiation temperature (T_r) of 294 eV (nearly 3.5 million degrees), see Figure 1. The x-ray drive is absorbed by a spherical sample mounted in the center of the hohlraum, in an outer region called the ablator. The ablator heats and expands, which launches inwardly converging shock waves via the rocket effect towards the center of the solid sphere. The shocks coalesce into a single stronger shock reaching near Gbar pressures at radii of $\sim$100μm. We measure the Hugoniot at the shock front as it travels inward, where the shock front pressure continuously increases due to convergence. The shock travels inward faster than the converging material behind it, enabling continuous tracking.

The density and pressure at the shock front are determined using temporally and spatially resolved streaked x-ray radiography measurements. The shock front speed is determined from the radiograph by tracking the shock front radial position as a function of time [20]. The radial density profile was extracted from the transmission of a 9 keV x-ray source (back-lighter) and analyzed via profile matching [19]. At these pressures, the opacity decreases from the cold opacity value due to carbon K-shell ionization. The opacity is simultaneously unfolded from the measured back-lighter transmission[24]. The mass density is further constrained by conserving the total mass contained within a higher opacity fiducial layer which is visible in the radiograph (radiographic Ge marker layer, see Fig.1b) and by matching the density profile to the known density of the un-shocked material ahead of the shock. Using Hugoniot jump relations we calculate the pressure, P, from the measured shock front speed, D, and the mass density, ρ[20,24],

$$P = P_0 + D^2\rho_0^2\left(\frac{1}{\rho_0} - \frac{1}{\rho}\right) \quad (1)$$

where ρ_0 is the initial mass density and P_0 is the initial pressure of the un-shocked material, see the Methods.

The experimental data is shown in Fig. 1d) where the shock front is labeled on the image. The shock travels at speeds of up to $150-220$ km/s, traversing the 1mm sample in $\sim$9 nanoseconds. We verify that the shock converges spherically by measuring the shock front symmetry to be within the radiographic resolution of 25μm at a shock radius of 200 μm through tracking of the radial density profiles on both sides of the sample in the equatorial plane. We also determine the symmetry through imaging of x-ray self emission at $\sim$9 nanoseconds when the shock wave collapses at the center of the sample (shock flash). Symmetry of the shock flash was measured to be within $0.5\pm0.3\mu$m at a shock radius of 12 μm in the equatorial direction via penumbral imaging[26].

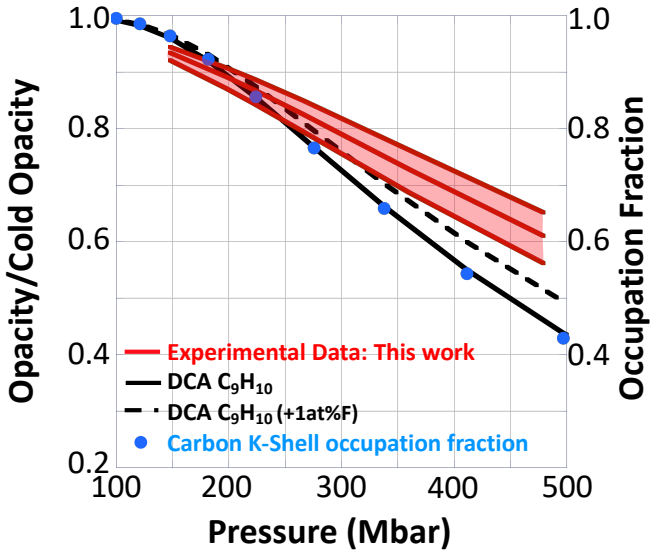

Figure 2 | Opacity of shock compressed C_9H_{10} at 9 keV Measured opacity at the shock front as a function of pressure along the shock Hugoniot (red curve and shaded region). Also plotted are theoretical curves of the normalized opacity vs pressure with and without 1at% F (black curves) along with the fraction of C K-shell occupation (blue circles) calculated using Detailed Configuration Accounting (DCA)[27].

Figure 2 shows the measured opacity at the shock front normalized to the cold material opacity (red curve) as a function of shock front pressure. Here, the red shaded region corresponds to uncertainty contours of $\pm1\sigma$ in the measurement. Also shown are calculations of the normalized opacity with and without trace amounts of fluorine present in the samples, see the Methods, using Detailed Configuration Accounting (DCA) [27] (black curves). Calculations of the carbon K-shell (inner shell) occupation fraction using DCA (blue circles) show that the calculated drop in opacity is directly correlated to the K-shell occupation, or ionization of the carbon K-shell. The measured opacities in these experiments are consistent with the modeling at pressures up to $\sim$300 Mbar and slightly higher than theory at higher pressures. The measured drop in opacity indicates significant distortion of the carbon inner shell with $\sim$63% occupation at 450Mbar.

The measured sequence of data points along the shock Hugoniot are shown in Fig. 3 (red curve) with error bars that correspond to uncertainty contours of 1σ (red shaded region). Also shown are previous shock Hugoniot measurements [18,28–30], theoretical calculations using Kohn-Sham Density Functional Theory (KS-DFT)-based molecular dynamics [31] (orange curve), and models using an Average Atom (AA) single ion-in-jellium description with the electronic structure based on Kohn-Sham Density Functional Theory (AA-DFT) [32–35,i] (solid black curve) and from Thomas-Fermi-Dirac theory (AA-TFD) [36,i] (dot-dashed black curve), see also the Methods. These models are commonly used to generate EOS tables for, e.g. inertial confinement fusion experiments.

[i] Equal pressure and temperature additive-volume prescriptions were used to mix the C and H contributions. For AA-TFD, both H and C were treated with Thomas-Fermi-Dirac theory. For AA-DFT the C EOS used ref. 34 and the H EOS used ref. 35.

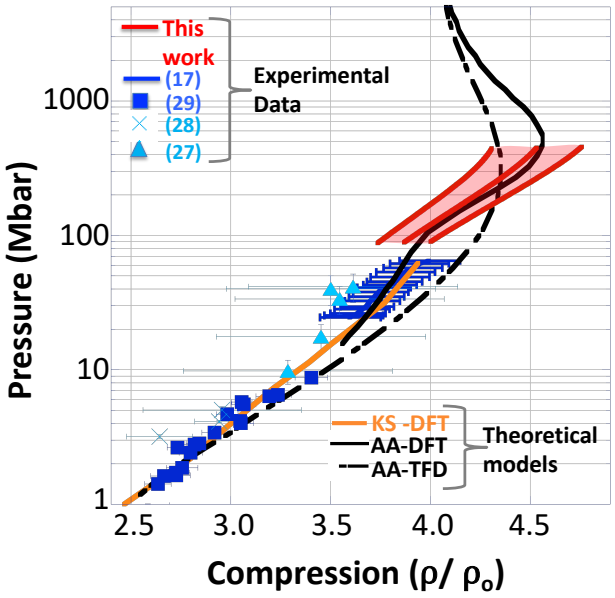

Figure 3 | C_9H_{10} **shock Hugoniot measurements**: Measured pressure vs mass density (ρ) normalized to the initial density (ρ_o) along the shock Hugoniot (red curve and shaded region). Also plotted are previous experimental data and theoretical modeling of the Hugoniot using Thomas-Fermi-Dirac theory (black dashed curve), average-atom Density Functional Theory (AA-DFT) (black curve), and Kohn Sham (KS)-DFT (orange curve).

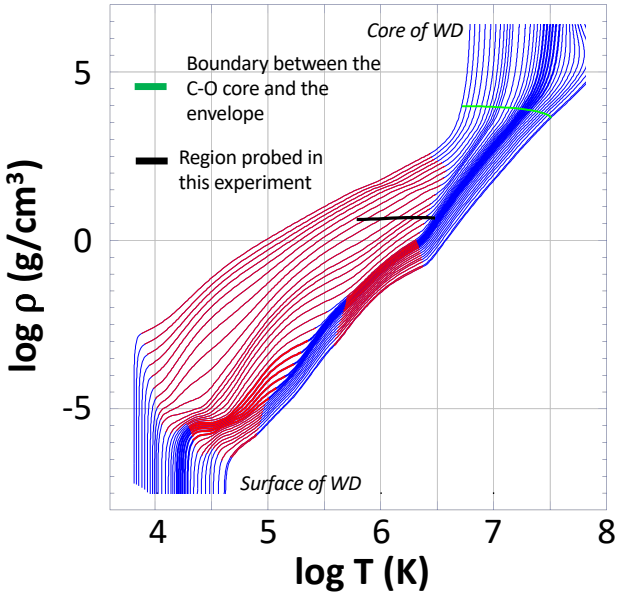

Figure 4 | Density-temperature diagram for the evolution of a white dwarf star with a mass of 0.6Msun composed of a carbon/oxygen core surrounded by a pure carbon envelope. Models start from hot and young state (right) and evolve leftward to older and colder structures, with the bold lines corresponding to hot DQ stars[3] . Convective regions in the stars are shown in red. The regime probed by the experiment is shown by the thick black line, with temperatures estimated from a model EOS[32–34].

The new extreme pressure measurements of the P-ρ Hugoniot presented in this work, for the first time, access the Hugoniot structure associated with the ionization of the carbon core electrons (K-shell). The shape of the Hugoniot in the range of ∼100-1000 Mbar is a result of the ionization of the core electrons of carbon (hydrogen being fully ionized under these conditions). First, ionization absorbs energy from the shock and the material becomes more compressible by an amount that depends on the interplay between the ionization energy and interactions in the plasma. Then, at higher pressures the curve swings back to lower compression due to reduced conversion of shock wave energy to internal degrees of freedom. Equations of state models that include the electronic shell structure (e.g.AA-DFT) show a sharper bend in the Hugoniot at these pressures and higher maximum compression than models that lack electronic shells (e.g. AA-TFD) and are in better agreement with the measurements. Path Integral Monte Carlo calculations are in general agreement with AA-DFT for hydrocarbons [10], and thus also accurately predict the shape of the high pressure Hugoniot and maximum compressibility for this hydrocarbon.

We provide data that, for the first time, accesses the conditions deep in the convection zone of hot DQ white dwarf (WD) stars. Figure 4 shows a sequence of interior models for the cooling of white dwarfs with a carbon-oxygen core and pure carbon envelope. As the star cools, its structure moves leftward in the diagram. Convectively unstable regions (in red) are associated with the partial ionization of carbon. The highest pressure-temperature experimental points reach the conditions of partial ionization of the core electrons of carbon that are similar to those at the bottom of the convection zone of hot DQ stars. This is the region most responsible for the driving of unstable pulsation modes[5,13] and where EOS models show the greatest range of variability. By constraining EOS models in this regime, these data can contribute to more accurate models of hot DQ stars, and a better understanding of their interior structures, pulsation properties, spectral evolution, and of their complex origin, thought to be from stellar mergers or through the late helium flash of asymptotic giant branch stars.

Methods Summary A formula for estimating the atomic pressure regime, a qualitative description of the radiographic analysis technique, reproducibility measurements, additional details on the experimental configuration and theoretical models, and additional details on pulsating white dwarfs are provided in the Methods.

Acknowledgements and Disclaimer This work performed under the auspices of the U.S. Department of Energy under Contract No. DE-AC52-07NA27344 and Contract no. 89233218CNA000001. This work has been supported by Laboratory Directed Research and Development (LDRD) award number 13-ERD-073. This work has also been supported by the University of California, Office of the President, Lab Fee Grant LFR-17-449059, by the Department of Energy, National Nuclear Security Administration, Award DE-NA0003842, and by the Department of Energy, Office of Science, Office of Fusion Energy Sciences, Award DE-SC0018298 and FWP 100182. We also acknowledge the NIF Discovery Science program for providing access to the facility. This document was prepared as an account of work sponsored by an agency of the United States government. Neither the United States government nor Lawrence Livermore National Security, LLC, nor any of their employees makes any warranty, expressed or implied, or assumes any legal liability or responsibility for the accuracy, completeness, or usefulness of any information, apparatus, product, or process disclosed, or represents that its use would not infringe privately owned rights. Reference herein to any specific commercial product, process, or service by trade name, trademark,

manufacturer, or otherwise does not necessarily constitute or imply its endorsement, recommendation, or favoring by the United States government or Lawrence Livermore National Security, LLC. The views and opinions of authors expressed herein do not necessarily state or reflect those of the United States government or Lawrence Livermore National Security, LLC, and shall not be used for advertising or product endorsement purposes. LLNL-JRNL-769585-DRAFT.

Data Availability The data that support the findings of this study are available from the corresponding author upon reasonable request.

Code Availability The data analysis algorithm that supports the findings of this study is available from author D.C.S. upon reasonable request.

1. N. Giammichele, S. Charpinet, G. Fontaine, P. Brassard, E. M. Green, V. Van Grootel, P. Bergeron, W. Zong and M.-a. Dupret, *Nature* **76**, 554 (2018).
2. D. E. Winget, C. J. Hansen, James Liebert, H. M. Van Horn, G. Fontaine, R. E. Nather, S. O. Kepler, and D. Q. Lamb, *The Astrophysical Journal* **315**, L77 (1987).
3. G. Fontaine, P. Brassard and P. Bergeron, *Publications of the Astronomical Society of the Pacific* **113**, 409 (2001).
4. Alejandro H. Corsico, Leandro G. Althaus, Marcelo M. Miller, Bertolami & S. O. Kepler, *The Astronomy and Astrophysics Review* **27**, (2019).
5. G. Fontaine, P. Brassard, and P. Dufour, *Astronomy & Astrophysics* **483**, L1 (2008).
6. D.E. Winget and S.O. Kepler, *Ann. Rev. Astron. Astrophys.* **46**, 157 (2008).
7. O. A. Hurricane, D. A. Callahan, D. T. Casey, P. M. Celliers, C. Cerjan, E. L. Dewald, T. R. Dittrich, T. Döppner, D. E. Hinkel, L. F. Berzak Hopkins, J. L. Kline, S. Le Pape, T. Ma, A. G. MacPhee, J. L. Milovich, A. Pak, H.-S. Park, P. K. Patel, B. A. Remington, J. D. Salmonson, P. T. Springer and R. Tommasini, *Nature* **506**, 343-348 (2014).
8. JA Gaffney, SX Hu, P Arnault, A Becker, LX Benedict, TR Boehly, PM Celliers, David M Ceperley, O ?ertk, J Clrouin, GW Collins, LA Collins, J-F Danel, N Desbiens, MWC Dharma-wardana, YH Ding, A Fernandez-Paella, MC Gregor, PE Grabowski, S Hamel, SB Hansen, L Harbour, XT He, DD Johnson, W Kang, VV Karasiev, L Kazandjian, MD Knudson, T Ogitsu, C Pierleoni, R Piron, R Redmer, G Robert, D Saumon, A Shamp, T Sjostrom, AV Smirnov, CE Starrett, PA Sterne, A Wardlow, HD Whitley, Brian Wilson, Ping Zhang, Eva Zurek, *High Energy Density Physics* **28**, 7-24 (2018).
9. D. Kraus, D. A. Chapman, A. L. Kritcher, R. A. Baggott, B. Bachmann, G. W. Collins, S. H. Glenzer, J. A. Hawreliak, D. H. Kalantar, O. L. Landen, T. Ma, S. Le Pape, J. Nilsen, D. C. Swift, P. Neumayer, R. W. Falcone, D. O. Gericke, and T. Döppner, *Phys. Rev. E* **94**, 011202 (2016).
10. S. Zhang, B. Militzer, L. X. Benedict, F. Soubiran, K. P. Driver, & P. A. Sterne, *J. Chem. Phys.* **148**, 102318 (2018).
11. D.C. Swift et al., Sensitivity of stars to the equation of state, *in preparation*.
12. P. Dufour, J. Liebert, G. Fontaine, and N. Behara, *Nature* **450**, 522 (2007).
13. P. Dufour, G. Fontaine, James Liebert, G. D. Schmidt, and N. Behara, *The Astrophysical Journal* **683**, 978 (2008).
14. G. Fontaine and H. M. Van Horn, *The Astrophysical Journal Supplement Series* **31**, 467 (1976).
15. Daniel S. Clark, Steven W. Haan, Bruce A. Hammel, Jay D. Salmonson, Debra A. Callahan, and Richard P. J. Town, *Physics of Plasmas* **17**, 052703 (2010).
16. B.A. Hammel, S.W. Haan, D.S. Clark, M.J. Edwards, S.H. Langer, M.M. Marinak, M.V. Patel, J.D. Salmonson, H.A. Scott, *High Energy Density Physics* **6**, 171 (2010).
17. A. S. Vladimirov, N. P. Voloshin, V. N. Nogin, A. V. Petrovtsev, V. A. and Simonenko, *JETP Lett.* **39**, 82-85 (1984).
18. Döppner, T., Swift, D., Kritcher, A., et al., *Phys. Rev. Lett.***121**, 025001 (2018).
19. D.C. Swift et al., LLNL Report No. LLNL-PROC-492261, 2011.
20. Damian C. Swift, Andrea L. Kritcher, James A. Hawreliak, Amy Lazicki, Andrew MacPhee, Benjamin Bachmann, Tilo Döppner, Joseph Nilsen, Gilbert W. Collins, Siegfried Glenzer, Stephen D. Rothman, Dominik Kraus, & Roger W. Falcone *Review of Scientific Instruments* **89**, 053505 (2018).
21. A.L. Kritcher, T. Döppner, D. Swift, J. Hawreliak, G. Collins, J. Nilsen, B. Bachmann, E. Dewald, D. Strozzi, S. Felker, O.L. Landen, O. Jones, C. Thomas, J. Hammer, C. Keane, H.J. Lee, S.H. Glenzer, S. Rothman, D. Chapman, D. Kraus, P. Neumayer, & R.W. Falcone, *High Energy Density Physics* **10**, 27 (2014).
22. R. F. Smith, J. H. Eggert, R. Jeanloz, T. S. Duffy, D. G. Braun, J. R. Patterson, R. E. Rudd, J. Biener, A. E. Lazicki, A. V. Hamza, J. Wang, T. Braun, L. X. Benedict, P. M. Celliers, & G. W. Collins, *Nature* **511**, 330 (2014).
23. Raymond F. Smith, Dayne E. Fratanduono, David G. Braun, Thomas S. Duffy, June K. Wicks, Peter M. Celliers, Suzanne J. Ali, Amalia Fernandez-Paella, Richard G. Kraus, Damian C. Swift, Gilbert W. Collins, & Jon H. Eggert , *Nature Astronomy* **2**, 452 (2018).
24. D.C. Swift et al., Simultaneous compression and opacity data from time-series radiography with a Lagrangian marker, *in preparation*.
25. E. Moses, R. Boyd, B. Remington, C. Keane, and R. Al-Ayat, Phys. Plasmas 16, 041006 (2009).
26. B. Bachmann, A. L. Kritcher, L. R. Benedetti, R. W. Falcone, S. Glenn, J. Hawreliak, N. Izumi, D. Kraus, O. L. Landen, S. Le Pape, T. Ma, F. Prez, D. Swift, & T. Döppner, *Rev Sci Instrum.* **85**, 11D614 (2014).
27. H. Scott and S. Hansen, *High Energy Density Physics* **6**, 39 (2010).
28. R. Cauble, T. S. Perry, D. R. Bach, K. S. Budil, B. A. Hammel, G. W. Collins, D. M. Gold, J. Dunn, P. Celliers, L. B. Da Silva, M. E. Foord, R. J. Wallace, R. E. Stewart, & N. C. Woolsey, *Phys. Rev. Lett.* **80**, 1248 (1998).
29. Ozaki, N., Sano, T., Ikoma, M., Shigemori, K., Kimura, T., Miyanishi, K., Vinci, T., Ree, F. H., Azechi, H., Endo, T., Hironaka, Y., Hori, Y., Iwamoto, A., *et al*, *Physics of Plasmas* **16** , 062702 (2009).
30. Barrios, M. A., Hicks, D. G., Boehly, T. R., Fratanduono, D. E. ,Eggert, J. H., Celliers, P. M., Collins, G. W. , & Meyerhofer, D. D., *Physics of Plasmas* **17** , 056307 (2010).
31. S. X. Hu, T. R. Boehly, & L. A. Collins, *Phys. Rev. E* **89**, 063104 (2014).
32. P.A. Sterne, L.X. Benedict, S. Hamel, A.A. Correa, J.L. Milovich, M.M. Marinak, P.M. Celliers, D.E. Fratanduono, *J. Phys.: Conf. Ser.* **717**, 012082 (2016).
33. B. Wilson, V. Sonnad, P. Sterne, W. Isaacs, *J. Quant. Spectrosc. Radiat. Transfer* **99**, 658 (2006).
34. Benedict, Lorin X., Driver, Kevin P., Hamel, Sebastien, Militzer, Burkhard, Qi, Tingting, Correa, Alfredo A., Saul, A., & Schwegler, Eric , *Phys. Rev. B* **89**, 224109 (2014).
35. G.I. Kerley, *Sandia National Laboratories Report, SAND2003 3613 (2003).*
36. Barnes and S. Lyon, *Documentation for Sesame table 7592 (unpublished, 1988).*

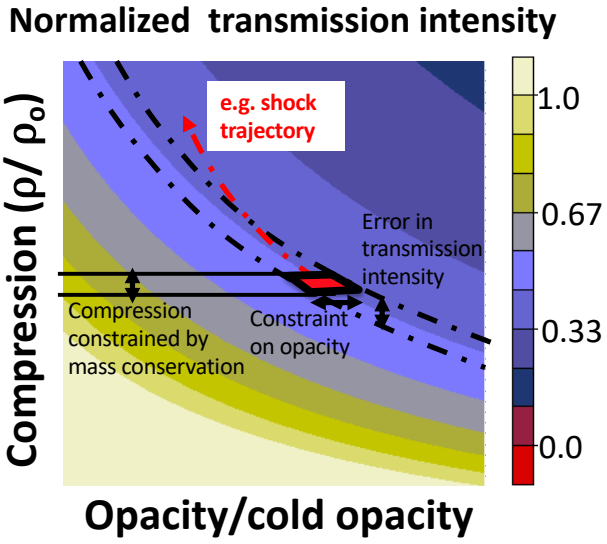

Figure 5 | Schematic of the radiographic analysis method: Normalized transmission intensity of an x-ray radiograph vs changes in compression and opacity. A given transmission corresponds to a range of possible compressions and opacities (black dashed curves). Density at the shock front is further constrained through knowledge of the initial material density ahead of the shock front and known mass contained within a region on the radiograph corresponding to a Ge marker layer in the sample. This further constrains the opacity and is done as the shock traverses the sample. An example shock trajectory is denoted with a red dashed curve.

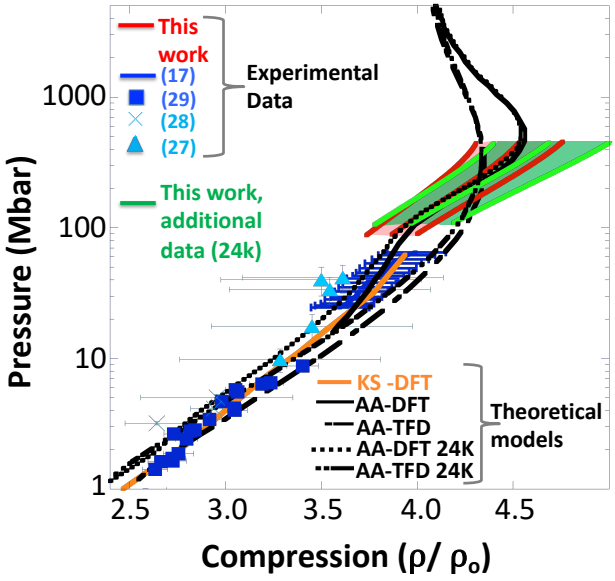

Figure 6 | Comparison of two C_9H_{10} shock Hugoniot measurements: Measured pressure vs mass density (ρ) normalized to the initial density (ρ_o) along the shock Hugoniot: green (data from shot N130103-009-999 fielded at 24K) and red (from Fig. 3, shot N130701-002-999 fielded at ambient temperature). Also plotted are the theoretical Hugoniots for AA-DFT and AA-TFD at 24K (ρ_o=1.136 g/cm^3), indicating that the initial density conditions are predicted to access approximately the same Hugoniot states at high pressure.

Methods

Atomic pressure regime

The atomic pressure regime is defined as the pressure required to significantly distort core electron orbitals, P_a, and can be estimated by

$$P_a = E_h / r_{Bohr}^3 = 294 Mbar \quad (2)$$

where E_h is the hartree energy and r_{Bohr} is the Bohr radius.

Simultaneous mass density and opacity unfold method

The measured transmission radiograph of an x-ray back-lighter source is sensitive to the mass density, or compression, and opacity of the sample material, see Fig.5. When the opacity of a material deviates significantly from the known cold opacity it must be considered to extract density information from the radiograph. Since there is no existing experimental measurements of the opacity of any material at the pressures in this work, we simultaneously extract the opacity from the radiograph. Here we use radial profile matching and optimization of the density and opacity to find best fits to the experimental data.

First, an initial guess of the density and opacity profiles are chosen based on physical parameters and radial transmission profiles are calculated. The calculated profiles are compared to the measured transmission profiles and are iterated until a good match to the experimental data is found. Uncertainty contours are determined from the quality of the profile fits to the radiograph. Since the relation between transmission intensity, mass density, and opacity is linear, additional information/assumptions are needed to constrain the range of profiles that provide a fit to the data. This is depicted in Figure 5, with a range of possible compressions and opacities that correspond to a given measured intensity (black dashed curves). Additional information for constraining the compression profile includes the known initial density ahead of the un-shocked material and known mass of the sample material inside of a Ge radiographic marker layer physically located inside the sample. This constraint on density provides a further constraint on the opacity. This is done continuously as a function of time as the shock traverses the sample. An example shock trajectory is shown in Fig.5 (red dashed curve). We also include an additional constraint that the opacity and density at the shock front vary smoothly in time and do not include discontinuous changes, see Ref. [24] for more details on the radiographic unfold analysis method and derived uncertainties.

The uncertainty contours of $\pm 1\sigma$ in the measurement shown in Figure 3 correspond to statistical uncertainty from simultaneously fitting of the parameterized opacity and density profiles to the measured radiograph. The parametrized fits were perturbed around the best fit and a probability distribution was constructed. This analysis includes uncertainty due to noise in the measurement. Systematic uncertainties from the magnification and the sweep speed of the x-ray streak camera correspond to $\sim$2% in compression and $\sim$7% in pressure, and mainly affect the location but not shape of the Hugoniot. The measurements in Fig. 3 and the additional measurements provided in the next section are consistent in both position and shape of the Hugoniot with AA-DFT.

Reproducibility

Figure 6 shows additional data obtained in this study in a separate experiment on NIF (green curves and green shaded region), included to demonstrate consistency of the analysis approach and to support our conclusions. This experiment (shot N130103-009-999) used the same sample material over a similar pressure range and was fielded at cryogenic temperatures (24K), with a measured initial density of 1.136 g/cm^3 consistent with the fielding temperature. The uncertainty contours of $\pm 1\sigma$ are larger than the main experiment shown in Figs. 3 & 6 (red curves and red shaded region) mainly as a result of using fewer laser beams to create the x-ray backlighter.

Figure 6 shows that a slightly higher density sample probes approximately the same theoretical shock Hugoniot at cryogenic temperatures as accessed at room temperature for both AA-DFT and AA-TFD over our pressure range. In the pressure range of these experiments the theoretical models deviate by roughly one percent in compression at the low pressure range and overlay at higher pressures.

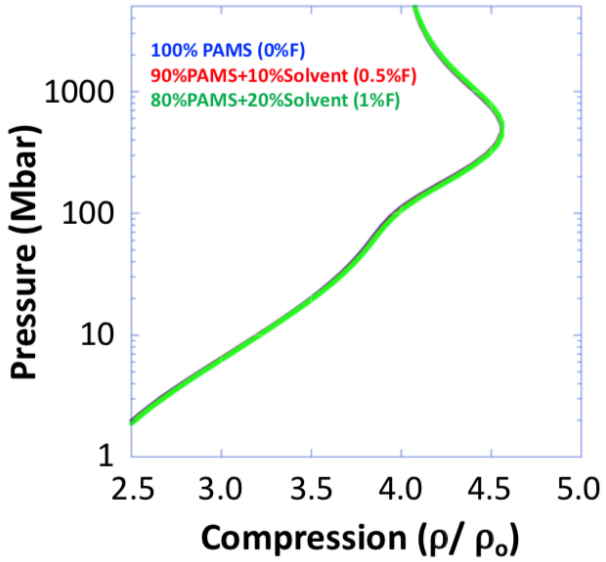

Figure 7 | Sensitivity of the theoretical Hugoniot to Fluorine: Calculations show insensitivity of the theoretical Hugoniot (AA-DFT[32–34]) to Fluorobenzene solvent (C_6H_5F) for concentrations up to 20%, corresponding to 1% atomic fraction of Fluorine (green curve). Concentrations of 0.5% F (red curve) and 0% F (blue curve) are also shown, but not visibly distinguishable.

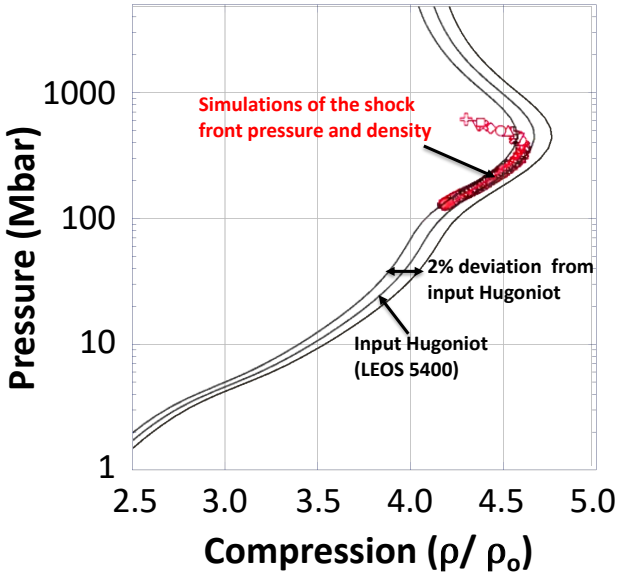

Figure 8 | Simulations of the shock front Hugoniot: Extracted shock front compressions and pressures from radiation Hydrodynamic simulations [37] of the experimental platform (red points). The theoretical shock Hugoniot [32–34] input to the simulations is also shown with ±2% deviation in compression from the input Hugoniot (black curves).

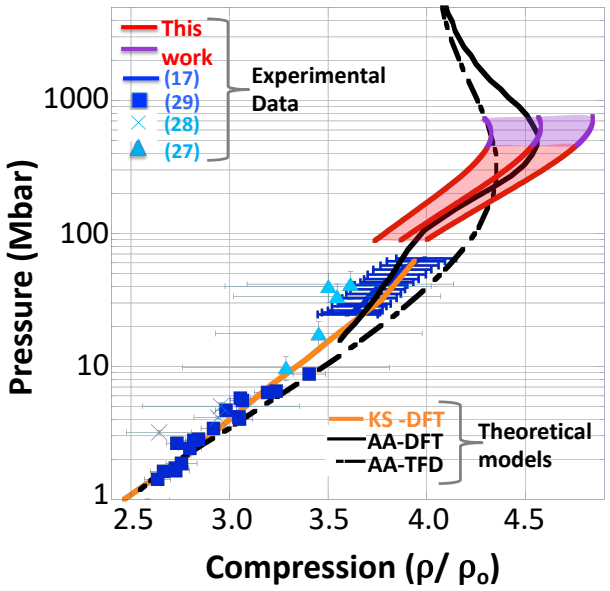

Figure 9 | Extended C_9H_{10} shock Hugoniot measurements: Measured pressure vs mass density (ρ) normalized to the initial density (ρ_o) along the shock Hugoniot from this work (red and purple curves and shaded region), where the purple curve corresponds to the extended data set that may be impacted by radiative shock front preheat. Also plotted are previous experimental data and theoretical modeling of the Hugoniot, see Fig. 3.

This additional data set is consistent with the data presented in Fig.2 with a difference of in the best fit compression of $<1\%$ at 107Mbar, $\sim 2\%$ at 300 Mbar, and $\sim 3\%$ at 450 Mbar. Both data sets show good agreement with models that include electronic structure in the AA-DFT approach.

Experimental configuration continued

The sample consisted of a solid sphere of Poly(Alpha Methyl-Styrene) (PAMS, C_9H_{10}) with trace amounts of fluorine (1at%) from the fabrication process uniformly distributed throughout the sphere, and a measured density of 1.085 $\pm$ 0.009 g/cm^3 fielded at ambient temperature. The fluorine concentration and uniformity were measured using Energy-dispersive X-ray Spectroscopy (EDS) and is calculated to have a negligible effect on the theoretical shock Hugoniot, see Fig.7. The spheres were coated with a plastic ablator (Glow Discharge Polymer) that included doped layers of Ge to mitigate x-ray preheat from the Hohlraum and act as a radiographic marker for the analysis. The laser drive was a two shock pulse shape with a total drive energy of 1.1MJ. The 9 keV, Zn He-α x-ray back-lighter was generated using up to 16 NIF laser beams incident on a Zn foil delayed in time relative to the drive beams, see Fig. 1 c). The main focus of the paper is on the analysis of NIF shot number N130701-002-999, but uses opacity information from NIF shot N130103-009-999 [24]. Radiation hydrodynamic simulations using HYDRA [37] benchmarked to shock timing data [38] calculate the shock coalescence of the two shocks inside the ablator to be before the Hugoniot points are extracted. Hot electron generation from laser-plasma interactions were inferred from measurements [39] to be an order of magnitude lower than previously observed with high pressure gas-fill hohlraums (He density of >0.96 mg/cm^3) by using a near vacuum hohlraum helium gas fill density of 0.03mg/cm^3. The calculated preheat of the sample inside the probed region as a result of the hot electrons is <1eV.

The estimated bulk sample preheat from the measured hohlraum x-ray background [40] is <1 eV inside the center of the sphere and <2.5 eV

at the outer probing radius of the sample, which does not cause the calculated shock Hugoniot to deviate significantly from the un-preheated Hugoniot [21] for these shock strengths. Simulations also indicate that radiative heating of the sample ahead of the shock from the shock itself is not significant for pressures up to ∼450 Mbar.

This can be seen in Figure 8 which includes extracted shock front densities and pressures from radiation hydrodynamic simulations of the experimental configuration (red points). Also plotted are curves of the input Hugoniot to the simulations [32–35] and ±2% deviation from the input Hugoniot. At lower pressures, ∼100 Mbar, the extracted Hugoniot deviates from the input Hugoniot due to bulk preheat from the hohlraum radiation drive at the level of $\leq$ 2%. Then, as the shock front pressure increases this level of preheat becomes a smaller perturbation on the Hugoniot and the extracted points follow the input Hugoniot more closely. At higher pressures of >450 Mbar, radiative preheat of material ahead of the shock front from the shock front itself starts to play a role. At 450 Mbar this preheating causes the Hugoniot to deviate from the input Hugoniot at the level of 2% in the direction of lower compression. We restrict the data record in Fig. 3 to ∼450 Mbar for this reason. At 720 Mbar these calculations suggest significantly lower compressions of 4.0 due to radiative preheat and deviation from the input Hugoniot of >12%. However, the full data range reaching pressures of ∼720 Mbar, shown in Fig. 9 (red and purple curves and shaded region), doesn't show this level of reduction in compression at high pressures which could be an indication that the modeling is overestimating radiative shock front preheat. Here, the central curves represent the best fit to experimental data and the shaded regions correspond to $\pm 1\sigma$ uncertainty.

Theoretical EOS models

The theoretical Hugoniot calculations for polystyrene presented in Fig. 3 for AA-DFT and AA-TF are equivalent to widely used EOS models for ICF experiments, see Figure 9 of *Gaffney, et al (2018)*[8]. Here, the AA-DFT model corresponds to EOS table LEOS 5112 which is the CH version of LEOS 5400 [41] (for glow discharge plastic), widely used to model ICF ablators. The AA-TF model corresponds to Sesame 7593, see *Gaffney, et al (2018)*[8] for a more detailed description.

Pulsating White Dwarfs

Hot DQ white dwarfs have an envelope composed of mostly carbon mixed with a modest amount of helium [12,13]. They are thought to result either from a late helium-shell flash in the post asymptotic giant branch evolution of stars or from stellar mergers. Most are highly magnetic and photometric variability has been attributed to the relatively rapid rotation of stellar spots in an out of view. However, some hot DQ stars are likely pulsators [42,43]. Our data will enable probing of the latter types.

37. M. M. Marinak, G. D. Kerbel, N. A. Gentile, O. Jones, D. Munro, S. Pollaine, T. R. Dittrich, and S. W. Haan, *Physics of Plasmas* **8**, 2275 (2001).
38. Berzak Hopkins, L. F. and Meezan, N. B. and Le Pape, et al, *Phys. Rev. Lett.* **114**, 175001 (2015).
39. Hohenberger M, Albert F, Palmer NE, Lee JJ, Döppner T, Divol L, Dewald EL, Bachmann B, MacPhee AG, LaCaille G, Bradley DK, & Stoeckl C, *Rev Sci Instrum.* **85**, 11D501 (2014).
40. E. L. Dewald, K. M. Campbell, R. E. Turner, J. P. Holder, O. L. Landen, S. H. Glenzer, R. L. Kauffman, L. J. Suter, M. Landon, M. Rhodes, & D. Lee, *Rev. Sci. Instrum.* **75**, 3759 (2004).
41. Sebastien Hamel, Lorin X. Benedict, Peter M. Cel-1396 liers, M. A. Barrios, T. R. Boehly, G. W. Collins, Tilo Do?ppner, J. H. Eggert, D. R. Farley, D. G. Hicks, J. L. Kline, A. Lazicki, S. LePape, A. J. Mackinnon, J. D. Moody, H. F. Robey, Eric Schwegler,, & Philip A. Sterne, *Phys. Rev. B* **86**, 094113 (2012).
42. A. H. Crsico, A. D. Romero, L. G. Althaus, and E. Garca-Berro, *Astronomy & Astrophysics* **506**, 835 (2009).
43. Montgomery M. H., Williams K. A., Winget D. E., Dufour P., DeGennaro S. and Liebert J., *Astrophysical Journal Letters* **678**, L51 (2008).